Electroless Deposition of Conformal Nanoscale Iron Oxide on Carbon Nanoarchitectures for Electrochemical Charge Storage

Megan B. Sassin,[†] Azzam N. Mansour,[‡] Katherine A. Pettigrew,[§] Debra R. Rolison,[†] and Jeffrey W. Long[†,]*

[†]Code 6170, Surface Chemistry Branch, Naval Research Laboratory, Washington, D.C. 20375, [‡]Systems and Materials for Power and Protection Branch, Naval Surface Warfare Center-Carderock Division, West Bethesda, Maryland 20817, and [§]Nova Research, Inc. 1900 Elkin Street, Suite 230, Alexandria, Virginia 22308

Mixed ion/electron-conducting transition metal oxides dominate the landscape of active cathode materials for electrical energy storage in secondary (*i.e.*, rechargeable) batteries, such as Li-ion batteries,[1–5] and are also being successfully adapted for use in electrochemical capacitors (ECs).[6–8] Oxides of nickel, cobalt, and manganese, and mixed oxides thereof, are among the most common materials used in Li-ion battery cathodes, while hydrous ruthenium oxides exhibit state-of-the-art pseudocapacitive charge storage for ECs.[9] Although these classes of metal oxides are well-established for electrochemical energy-storage applications, the development of new active materials continues with an emphasis on achieving enhanced stability, charge-storage capacity, and/or high-voltage operation. The costs and environmental impact of state-of-the-art battery/EC oxides based on nickel, cobalt, and ruthenium oxides are also driving the search for alternative charge-storage materials, including LiFePO$_4$ and related lower-cost materials.[10,11]

Iron oxides are a class of materials that are potentially advantageous for batteries and electrochemical capacitors owing to their low cost and low toxicity. Although iron oxides have not been as extensively studied for batteries and ECs as other metal oxides, recent work has demonstrated that certain forms of iron oxides can be used as both the active cathode[12–16] and anode[17,18] material for Li-ion batteries, and also as a negative electrode material for aqueous asymmetric ECs.[19–23] The electrochemical performance of conventional forms of iron oxide is not yet competitive, but its charge-

ABSTRACT We describe a simple self-limiting electroless deposition process whereby conformal, nanoscale iron oxide (FeO$_x$) coatings are generated at the interior and exterior surfaces of macroscopically thick ($\sim$90 μm) carbon nanofoam paper substrates *via* redox reaction with aqueous K$_2$FeO$_4$. The resulting FeO$_x$-carbon nanofoams are characterized as device-ready electrode structures for aqueous electrochemical capacitors and they demonstrate a 3-to-7 fold increase in charge-storage capacity relative to the native carbon nanofoam when cycled in a mild aqueous electrolyte (2.5 M Li$_2$SO$_4$), yielding mass-, volume-, and footprint-normalized capacitances of 84 F g^{-1}, 121 F cm^{-3}, and 0.85 F cm^{-2}, respectively, even at modest FeO$_x$ loadings (27 wt %). The additional charge-storage capacity arises from faradaic pseudocapacitance of the FeO$_x$ coating, delivering specific capacitance >300 F g^{-1} normalized to the content of FeO$_x$ as FeOOH, as verified by electrochemical measurements and *in situ* X-ray absorption spectroscopy. The additional capacitance is electrochemically addressable within tens of seconds, a time scale of relevance for high-rate electrochemical charge storage. We also demonstrate that the addition of borate to buffer the Li$_2$SO$_4$ electrolyte effectively suppresses the electrochemical dissolution of the FeO$_x$ coating, resulting in <20% capacitance fade over 1000 consecutive cycles.

KEYWORDS: iron oxide · electrochemical capacitor · battery · charge storage · pseudocapacitance · aerogel

storage capacity improves markedly when synthesized in high-surface-area, nanoscale forms.[21,24,25]

The electrochemical properties of nanoscale iron oxides may be further enhanced by distributing them as coatings onto high-surface-area, electrically conductive carbon substrates, as we recently described for manganese oxides deposited as conformal nanoscale coatings onto carbon-paper-supported nanofoam structures.[26,27] In the present report, we describe a related deposition strategy in which we use the redox reaction between the strong oxidant potassium ferrate (K$_2$FeO$_4$)[28] and the carbon nanofoam substrate to generate conformal, nanoscale FeO$_x$ coatings on the interior and exterior carbon surfaces of the nanofoam. We further demonstrate that the resulting nanoscale FeO$_x$ coatings are

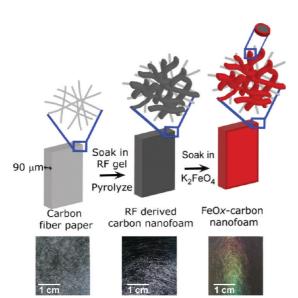*Address correspondence to jeffrey.long@nrl.navy.mil.

Figure 1. FeO$_x$-carbon nanofoam fabrication scheme (top) and optical images of carbon fiber paper (bottom left), carbon nanofoam (bottom middle), and FeO$_x$-carbon nanofoam (bottom right).

electroactive in a mild aqueous electrolyte (2.5 M Li$_2$SO$_4$) and exhibit pseudocapacitance that increases the gravimetric (3×), volumetric (7×), and footprint-normalized (7×) capacitance relative to that of the native carbon nanofoam.

RESULTS AND DISCUSSION

The deposition of nanoscale iron oxides onto high-surface-area carbon powders *via* solution-based coprecipitation methods has been previously reported.[19,29] Modifying carbon powders dispersed in a liquid with FeO$_x$ is a synthetically simple strategy; however, covering the good electron conductor (carbon powder) with coatings of FeO$_x$ (poor electron conductor) proves problematic when the oxide-modified carbon is subsequently processed into a composite electrode structure. Long-range electron paths must then be re-established by the addition of unmodified carbon to the composite structure, ultimately diluting and potentially limiting electrolyte access to the active FeO$_x$ phase. In our work, the carbon substrate is a fiber-paper-supported nanofoam of macroscopic dimensions (geometric area of many cm^2; thickness ≈ 90 μm),[30,31] a device-ready form factor that also maintains uninterrupted electron paths to the nanoscale FeO$_x$ deposits, but which presents new challenges for achieving homogeneous deposition of conformal FeO$_x$ coatings throughout the tortuous void volume of the preformed carbon nanofoam (see schematic in Figure 1). To retain the through-connected aperiodic pore structure of the native carbon nanofoam and to avoid build-up of thick FeO$_x$ coatings on the exterior of the nanofoam, it is imperative to identify deposition conditions where the FeO$_x$ precursor, in this case K$_2$FeO$_4$, reacts preferentially with the carbon until the resulting FeO$_x$ coating passivates the surface

to further reaction, while also minimizing extraneous reactions in solution that may result in FeO$_x$ precipitates and/or thick exterior coatings.

Potassium ferrate is a strong oxidant (E ≈ +0.7 V at pH 14),[28] and thus an attractive precursor for electroless FeO$_x$ deposition, but its solvated form is only stable in alkaline solutions of a narrow pH range. After several iterations, we determined that a precursor solution of 25 mM K$_2$FeO$_4$ in 9 M KOH provides the optimal balance between stability of the ferrate precursor in solution and its reactivity toward the carbon surfaces of the nanofoam. To perform the depositions, nanofoam papers were infiltrated with the aqueous alkaline ferrate solution and allowed to react for either 20 or 40 h, followed by rinsing and drying. The gravimetric mass uptake of the 20-h and 40-h FeO$_x$-carbon nanofoams was 25 wt % and 50 wt %, respectively. Elemental analysis of these materials showed that the Fe content was 10 wt % after a 20-h deposition and increased to 17 wt % after 40 h. Assuming an oxide formula of FeOOH (see the following sections on the structural characterization of these materials), the elemental analysis translates to 16 wt % FeOOH and 27 wt % FeOOH for 20-h and 40-h depositions, respectively. The approximately 2-fold discrepancy between the gravimetric weight loading and the Fe elemental analysis results can be explained by additional mass resulting from carbon–oxygen functionalities that are generated at the carbon surfaces upon reaction with the strongly oxidizing K$_2$FeO$_4$[32] (see X-ray photoelectron spectroscopy characterization in Supporting Information), incorporation of K$^+$ from the precursor solution (see elemental analysis results in Supporting Information), and the presence of physisorbed H$_2$O associated with the hydrophilic FeOOH coating.

Scanning electron microscopy (SEM) and energy-dispersive X-ray spectroscopy (EDS) studies of the carbon nanofoams before and after reaction with the alkaline K$_2$FeO$_4$ precursor solution confirm that homogeneous, nanoscale FeO$_x$ coatings are generated throughout the macroscopic thickness (90 μm) of the preformed carbon nanofoam, while the aperiodic pore structure of the native nanofoam is also preserved (see Figure 2). The FeO$_x$ forms as a thin ribbon-like deposit at both the exterior and interior walls of the carbon nanofoam, which itself exhibits a sponge-like structure. The ribbon-like FeO$_x$ morphology is further verified by transmission electron microscopy (TEM), where the oxide is differentiated from the carbon substrate by its greater Z-contrast under the electron beam (see Figure 3, left panel).

The intimate contact between the oxide and the carbon is demonstrated by high-resolution TEM (HR-TEM), in that no distinct separation of the two materials is evident for the FeO$_x$-coated regions (see Figure 3, right panel; large-area HR-TEM images are included in Supporting Information). Note that the overlap of the FeO$_x$
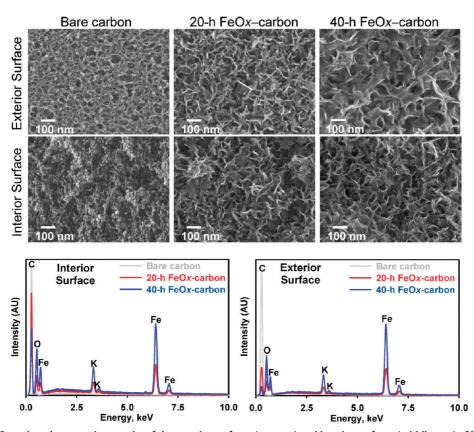
Figure 2. Scanning electron micrographs of the exterior surfaces (top row) and interior surfaces (middle row) of bare carbon nanofoam (left), 20-h FeO$_x$-carbon nanofoam (middle), and 40-h FeO$_x$-carbon nanofoam (right). Energy-dispersive X-ray (bottom row) of the interior surfaces (left) and exterior surfaces (right) of carbon nanofoam (gray), 20-h FeO$_x$-carbon nanofoam (red), and 40-h FeO$_x$-carbon nanofoam (blue).

and carbon domains can be discerned by a gradual change in intensity of the gray scale and lack of lattice fringes. Occasionally the location of the oxide domain near an edge allows distinct lattice fringes of the oxide to be discerned (see Figure 3, right panel). The distinct contrast in the TEM image shows that, although homogeneously distributed within the nanofoam structure, the FeO$_x$ does not exhaustively coat all carbon surfaces.

Nitrogen-sorption porosimetry was used to track the changes in specific surface area, pore volume, and pore-size distribution after FeO$_x$ deposition (Table 1). Both bare carbon and FeO$_x$-coated carbon nanofoams exhibit Type II nitrogen-sorption isotherms, characteristic of a mesoporous structure, with decreasing specific nitrogen physisorption as the FeO$_x$ is incorporated into the carbon nanofoam (Figure 4A). Specific surface areas decreased from 533 m^2 g^{-1} for the bare carbon nanofoam to 431 m^2 g^{-1} for the 40-h FeO$_x$-coated carbon nanofoam, while the cumulative pore volume also decreased with the incorporation of FeO$_x$, from 0.79 cm^3 g^{-1} for the bare carbon nanofoam to 0.51 cm^3 g^{-1} for the 40-h FeO$_x$-carbon nanofoam (Table 1). As would be expected for incorporation of FeO$_x$ coatings within the bare carbon nanofoam interior, the mean pore size and total pore volume decreased with longer FeO$_x$ deposition times (and concomitant higher FeO$_x$ weight loadings), as shown in Table 1 and Figure

4B. Pore-size distribution plots generated from the isotherm data show that the width of the pores gradually shifts to smaller sizes with increasing FeO$_x$ content, yet even the 40-h FeO$_x$-coated carbon nanofoam retains a through-connected pore network, with pore sizes ranging from ca. 3–15 nm.

The electrochemical properties of the bare and FeO$_x$-coated carbon nanofoams were examined in a half-cell configuration, using an aqueous electrolyte (2.5 M Li$_2$SO$_4$) and a potential window of relevance (+0.2 ↔ −0.8 V vs Ag/AgCl) for their ultimate use as negative electrodes in aqueous electrochemical capacitors, for example, when paired with a MnO$_2$-based positive
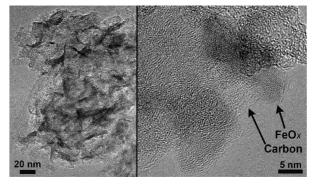

Figure 3. Transmission electron micrographs of 40-h FeO$_x$-carbon nanofoam at low magnification (left) and at high magnification (right).

TABLE 1. Summary of the Physical and Electrochemical Properties of Native Carbon and FeO$_x$-Coated Carbon Nanofoams

sample	weight % Fe	BET surface area[a] (m^2 g^{-1})	cumulative pore volume[a] (cm^3 g^{-1})	mean pore size[a] (nm)	specific capacitance[b] (F g^{-1})	volumetric capacitance[b] (F cm^{-3})	area-normalized capacitance[b] (F cm^{-2})
bare carbon	NA	533	0.79	9.7	31	17	0.12
20-h FeO$_x$	10	481	0.63	7.3	54	40	0.28
40-h FeO$_x$	17	431	0.51	6.5	84	121	0.85

[a]Typical deviation in the porosimetry values as derived from replicate analyses is ±5%. [b]Typical experimental deviation in the capacitance values is ±5%.

electrode.[21−23] Representative cyclic voltammograms for the bare carbon nanofoam and FeO$_x$-carbon nanofoams are shown in Figure 5A. All three nanofoams exhibit a semirectangular shape that is indicative of capacitive or pseudocapacitive behavior, with no evidence of resistance limitations arising from the poorly conductive FeO$_x$ coating at a scan rate of 5 mV s^{-1} (see cyclic voltammograms at scan rates up to 100 mV s^{-1} in Supporting Information), thereby providing further evidence that the underlying carbon nanofoam structure is an effective current conductor to the nanoscale FeO$_x$ domains. Improved charge storage upon incorporation of the pseudocapacitive FeO$_x$ coatings is evident in this voltammetric comparison (see Figure 5A), with specific capacitance increasing with increasing FeO$_x$ content (see Table 1).
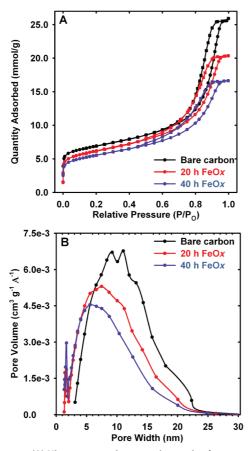

Figure 4. (A) Nitrogen-sorption porosimetry isotherms and (B) pore size distributions of bare carbon nanofoam (black), 20-h FeO$_x$-carbon nanofoam (red), and 40-h FeO$_x$-carbon nanofoam (blue).

The specific capacitance (normalized to total electrode mass) increases from 31 F g^{-1} for the bare carbon nanofoam to 54 and 84 F g^{-1} for the 20-h and 40-h FeO$_x$-carbon nanofoam, respectively—normalizing these specific capacitance values to the FeOOH mass determined by elemental analysis yields 343 and 314 F g$_{FeOOH}^{-1}$, respectively. By comparison, prior studies in aqueous electrolytes with FeO$_x$-based electrodes (thin films and powder−composite forms as well as various FeO$_x$ polymorphs) have reported FeO$_x$-normalized capacitances ranging from 5 to 146 F g^{-1} (see Table S1 in Supporting Information).[19−21,24,25,33] One exception was reported by Wu et al. where 510 F g$_{Fe_3O_4}^{-1}$ was achieved, but only under very limiting circumstances: a low oxide weight loading (3 wt %), which resulted in only 40 F g^{-1} normalized to the Fe$_3$O$_4$-carbon composite mass and using a sulfite-based aqueous electrolyte, which is not ideal for asymmetric ECs due to interference from the electrochemical oxidation of the sulfite anion, which would limit the available voltage window at the positive electrode of an asymmetric EC using such aqueous electrolytes (see Supporting Information).[19]

In the present case, we posit that the high FeO$_x$-based specific capacitance exhibited by the FeO$_x$-carbon nanofoam is a consequence of the "multifunctional nanoarchitecture" design,[34] where the nanoscale FeO$_x$-coating is in intimate contact with both the 3-D current collector (the carbon nanofoam) and the electrolyte that permeates the through-connected pore network of the nanofoam. With this particular electrode design, while the specific capacitance is increased by a factor of ∼3 after FeO$_x$ deposition, greater improvements in volumetric and geometric (footprint-normalized) capacitance are observed because the FeO$_x$ coating provides pseudocapacitance without increasing the footprint or volume of the native carbon nanofoam. For example, both the volumetric and footprint-normalized capacitance increase by a factor of 7 for a 40-h FeO$_x$-carbon nanofoam relative to the native carbon nanofoam (see Table 1).

In light of their prospective use as negative electrode materials in asymmetric ECs with mild aqueous electrolytes, the FeO$_x$-normalized specific capacitance is highly promising, yet the modest FeO$_x$ weight loadings limit the total electrode-normalized specific capacitances. By comparison, composite electrode structures
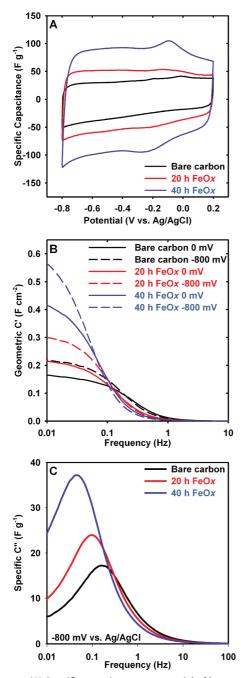
Figure 5. (A) Specific capacitance *vs* potential of bare carbon nanofoam (black), 20-h FeO$_x$-carbon nanofoam (red), and 40-h FeO$_x$-carbon nanofoam (blue) in 2.5 M Li$_2$SO$_4$ at 5 mV s^{-1}. (B) Bode plot of the real component of the capacitance normalized to the geometric area of the electrode of bare carbon nanofoam (black), 20-h FeO$_x$-carbon nanofoam (red), and 40-h FeO$_x$-carbon nanofoam (blue) in 2.5 M Li$_2$SO$_4$ at 0 mV (solid lines) and −800 mV (dashed lines) *vs* Ag/AgCl. (C) Bode plot of the imaginary component of the capacitance normalized to the electrode mass of bare carbon nanofoam (black), 20-h FeO$_x$-carbon nanofoam (red), and 40-h FeO$_x$-carbon nanofoam (blue) in 2.5 M Li$_2$SO$_4$ at −800 mV *vs* Ag/AgCl.

of high-surface-area carbons are themselves typically limited to *ca*. 100−130 F g^{-1} in similar mild aqueous electrolytes,[22,35,36] although these same carbons would exhibit much higher specific capacitances in either strongly basic or strongly acidic electrolytes.[37] We an-

ticipate that further optimization of the electroless deposition conditions and fine-tuning of the carbon nanofoam pore structure, particularly targeting pores in the 50-to-100 nm range, should result in greater FeO$_x$ mass loadings and correspondingly higher total specific capacitance, while maintaining the advantages of the current FeO$_x$-carbon nanofoam design for rate-critical applications. As a preliminary example, we extended the 20-h FeO$_x$ deposition protocol to a different nanofoam substrate with larger pore sizes (5−60 nm), which resulted in an increase in the gravimetric weight uptake from 25 to 34 wt % and an increase in the total electrode specific capacitance from 54 to 65 F g^{-1} for the carbon nanofoam with the larger pores (see Supporting Information).

High-rate operation is a key characteristic of electrochemical capacitors and as such electrochemical impedance spectroscopy was used to explore the frequency-dependence of the FeO$_x$ pseudocapacitance. Typical Bode plots of the real component of the AC capacitance (normalized to the geometric area) at two DC potentials (0 and −800 mV *vs* Ag/AgCl) are shown in Figure 5B. At both potentials the low-frequency capacitance increases with increasing FeO$_x$ content, consistent with the cyclic voltammetric results. At 0 mV, the geometric capacitances of the 20-h and 40-h FeO$_x$-carbon nanofoams converge to that of the bare carbon nanofoam at ∼0.1 Hz, beyond which the additional capacitance contributed by the FeOOH component of the FeO$_x$-carbon nanofoam is no longer accessible. At −800 mV, the capacitance of the 40-h FeO$_x$-carbon nanofoam decreases rapidly and converges with the bare carbon nanofoam at ∼0.09 Hz, while the capacitance of the 20-h FeO$_x$-carbon is still accessible at ∼0.1 Hz. The electrode response time can be estimated from the frequency of the maxima of a Bode plot of the imaginary capacitance. As expected, as the FeO$_x$ content increases, the response time increases from 10 (20-h FeO$_x$) to 22 s (40-h FeO$_x$) as shown in Figure 5C. The increase in response time with increase in FeO$_x$ content is a consequence of a larger RC time constant for the electrode structure, which results from a significant increase in electrode capacitance but only a modest increase in electrode resistance (∼1 Ω cm^2 greater real impedance for FeO$_x$-coated nanofoam *vs* the bare carbon nanofoam; see Nyquist plots in Supporting Information).

We used X-ray absorption spectroscopy (XAS) to determine the Fe oxidation state and local Fe−O atomic structure in the as-deposited state as well as during electrochemical cycling of the FeO$_x$-carbon nanofoam in an *in situ* cell. On the basis of comparisons of the X-ray absorption near-edge structure (XANES) spectra (Figure 6A) and especially the pre-edge regions (Figure 6A inset) of FeO, Fe$_3$O$_4$, α-Fe$_2$O$_3$, γ-Fe$_2$O$_3$, and amorphous FeOOH, we conclude that the oxidation state of Fe in the as-deposited FeO$_x$-carbon nanofoam is close
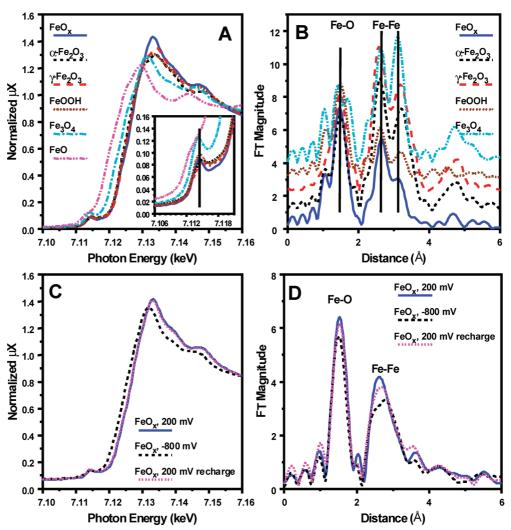
Figure 6. (A) *Ex-situ* Fe K-edge XANES and pre-edge region (inset in A) and (B) Fourier transforms of k^3-weighted EXAFS spectra over the range $2.5-14$ Å^{-1} for the as-deposited nanoscale 20-h FeO$_x$-carbon nanofoam along with those for reference standards α-Fe$_2$O$_3$, γ-Fe$_2$O$_3$, amorphous FeOOH, and Fe$_3$O$_4$. (C) *In-situ* Fe K-edge XANES and (D) Fourier transforms of k^3-weighted EXAFS spectra over the range $3.0-11$ Å^{-1} of a 20-h FeO$_x$-carbon nanofoam electrode conditioned at 200 mV, discharged to -800 mV, and recharged to 200 mV *vs* Ag/AgCl.

to $+3$ and its local coordination geometry is similar to that of Fe in the amorphous FeOOH standard material.[38−40] Extended X-ray absorption fine-structure (EXAFS) analysis confirmed that the positions of the Fourier-transform peaks for the as-deposited FeO$_x$-carbon nanofoam are similar to those of amorphous FeOOH, but their intensities are somewhat higher (Figure 6B), indicating a higher degree of order for the conformal ribbons of FeOOH formed in the FeO$_x$-carbon nanofoam, than that formed in the amorphous FeOOH standard.

In-situ X-ray absorption spectroscopy under electrochemical control was performed to elucidate the charge-storage mechanism of the FeO$_x$-based pseudocapacitance in aqueous 2.5 M Li$_2$SO$_4$. The XANES and EXAFS spectra were collected after the 20-h FeO$_x$-carbon electrode was charged and discharged at specific potentials ranging from 0.2 to -0.8 V *vs* Ag/AgCl. The edge energy shifted from 7124.12 to 7122.83 eV upon discharging from $+0.2$ to -0.8 V confirming re-

duction of Fe^{3+} (Figure 6C). With the use of the observed edge energy of the FeO standard as a reference for Fe^{2+} and the edge energy of FeOOH as a reference for Fe^{3+}, the change in edge energy per unit valency is estimated to be 4.42 eV. Hence, the change in oxidation state of Fe upon discharging from $+0.2$ to -0.8 V is -0.29. As can be seen from comparisons of Fourier transforms (Figure 6D), the local structure of Fe is not significantly perturbed upon reduction of the oxide by ~0.3 electrons per Fe. The decrease in the amplitude of the Fe$-$O shell and the slightly higher average Fe$-$Fe distance upon discharging to -0.8 V are consistent with reduction of a fraction of Fe^{3+} sites to Fe^{2+}.

Upon recharging the electrode from -0.8 to $+0.2$ V, the XANES spectra (Figure 6C) revealed that the Fe oxidation state reversibly toggled between ~3.0 and 2.7. Assuming an Fe oxidation state change of 0.3 as determined by XANES, an FeOOH composition, and the 1-V potential window examined, we calculate an expected specific capacitance of 325 F g$_{FeOOH}^{-1}$, which is highly
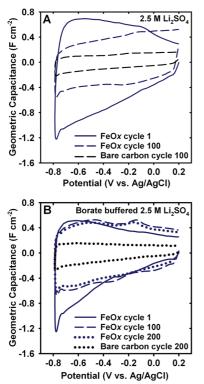
Figure 7. Geometric capacitance *vs* potential in (A) 2.5 M Li$_2$SO$_4$ at 5 mV s^{-1} and in (B) buffered 2.5 M Li$_2$SO$_4$ at 5 mV s^{-1} of cycle 100 for bare carbon nanofoam (black dotted line) and cycles 1 (solid blue line), 100 (blue dashed line), and 200 (blue dotted line) for 40-h FeO$_x$-carbon nanofoam.

consistent with the 343 F g$_{FeOOH}$$^{-1}$ determined by cyclic voltammetry for the 20-h FeO$_x$-carbon nanofoam. As can be seen from Figure 6C, the XANES spectrum of the electrode recharged from −0.8 to +0.2 V is completely restored to the spectrum recorded for the same electrode at +0.2 V prior to discharge, thereby indicating the reversibility of the FeOOH pseudocapacitance reaction during this initial electrochemical cycling. While the XANES data demonstrate that the pseudocapacitance of the FeOOH coating arises from a reversible Fe^{3+}/Fe^{2+} redox couple, the identity of the charge-compensating cation (Li$^+$ and/or H$^+$) involved in the pseudocapacitance reaction is as yet undetermined.

The electrochemical stability of FeO$_x$ in relevant aqueous electrolytes is a crucial issue that must be addressed in order to validate the use of the oxide for electrochemical capacitor applications, for example, when

paired as a negative electrode with a MnO$_2$-based positive electrode in an asymmetric cell configuration with a mild aqueous electrolyte.[21−23] In the present case, we used lithium sulfate as the electrolyte salt due to its high solubility and the high ionic conductivity of the resulting aqueous electrolytes (∼80 mS cm^{-1} at 2.5 M). However, at such concentrations, aqueous lithium sulfate does not form a "neutral-pH" solution, but exhibits a pH of ∼3.5. The acidity of the lithium sulfate electrolyte is expected to promote reductive dissolution of the FeO$_x$ when cycled to progressively negative potentials, with the formation of soluble Fe^{2+} species and loss of active FeO$_x$.[41,42] In fact, we observe a 42% decrease in the specific capacitance for a 40-h FeO$_x$-carbon nanofoam at cycle 100 in 2.5 M Li$_2$SO$_4$ (Figure 7A, Table 2).

Ex situ XAS experiments performed on 40-h FeO$_x$-carbon nanofoams after 10, 25, 50, and 100 voltammetric cycles in 2.5 M Li$_2$SO$_4$ confirm that there is significant loss of Fe from the electrode after cycling in 2.5 M Li$_2$SO$_4$, with most of the degradation occurring from cycle 50 to cycle 100, while the FeOOH-like local structure of the remaining FeO$_x$ is retained (see Supporting Information). These results confirm that the decrease in capacitance is due to a slow dissolution of FeO$_x$ and not because of any irreversible FeO$_x$ phase changes to electrochemically inactive forms. The presence of soluble Fe^{2+} in the 2.5 M Li$_2$SO$_4$ electrolyte after 100 cycles of the FeO$_x$-carbon nanofoam electrode was qualitatively confirmed by the addition of the colorimetric indicator, phenanthroline, to an aliquot of the electrolyte postcycling (see photograph in Supporting Information). The FeO$_x$ dissolution and associated capacitance fade with cycling can be minimized by simply adding a buffering agent to the electrolyte to increase the pH. In the present case, we added 50 mM sodium borate, which stabilizes the pH of the 2.5 M Li$_2$SO$_4$ at 8.5. The specific capacitance of a 40-h FeO$_x$-carbon nanofoam in this borate-buffered electrolyte exhibited only a 10% decrease over 200 cycles (Figure 7B, Table 2) and a 20% decrease over 1000 cycles (see cyclic voltammograms in Supporting Information). Colorimetric analysis of the borate-buffered 2.5 M Li$_2$SO$_4$ electrolyte with added phenanthroline after 1000 cycles of the 40-h FeO$_x$-carbon nanofoam electrode yielded a colorless solution, indicating that reductive dissolution

TABLE 2. Specific Capacitance for Bare Carbon and 40-h FeOx-Carbon Electrodes at Selected Cycles in Li$_2$SO$_4$ and Borate-Buffered Li$_2$SO$_4$ during Extended Voltammetric Cycling

	specific capacitance cycle 1 (F g$_{total}$$^{-1}$)	specific capacitance cycle 200 (F g$_{total}$$^{-1}$)	specific capacitance cycle 1000 (F g$_{total}$$^{-1}$)
2.5 M Li$_2$SO$_4$			
bare carbon	31	27	N/A
40-h FeO$_x$-carbon	85	49	N/A
Borate-Buffered 2.5 M Li$_2$SO$_4$			
bare carbon	26	19	N/A
40-h FeO$_x$-carbon	72	65	58

of Fe^{2+} is effectively suppressed by the presence of the borate buffer (see photo in "Supporting Information"). Additional work is ongoing to further improve the chemical and electrochemical durability of these FeO_x-based materials in aqueous electrolytes of relevance for EC applications.

CONCLUSIONS AND OUTLOOK

We present a facile and scalable method to incorporate conformal, nanoscale, electroactive coatings of FeO_x within the complex pore—solid architectures of carbon nanofoam papers. Preliminary electrochemical results demonstrate that the FeO_x coatings exhibited faradaic pseudocapacitance reactions that substantially enhanced the charge-storage capacity of the native carbon nanofoams when cycled in mild aqueous electrolytes. Further optimization and fine-tuning of both the electroless deposition conditions and pore structure and density of the carbon nanofoam substrate should result in even greater FeO_x mass loadings, thereby yielding correspondingly higher specific capacitance, while retaining conformal, nanometric coatings. The FeOOH-type nanoscale coatings achieved with this electroless deposition method can also be converted *via* thermal processing to various nanocrystalline FeO_x forms (*e.g.*, Fe_3O_4, α-Fe_2O_3, or γ-Fe_2O_3)[43] that will be of interest for other applications including Li-ion batteries, electrocatalysis, and heterogeneous catalysis.

EXPERIMENTAL METHODS

Carbon Nanofoam Synthesis. Fiber-supported carbon nanofoam papers were produced by adapting previously published methods of Pekala *et al.*[30] In a typical synthesis, 6.6 g of resorcinol (Sigma Aldrich, Reagent Plus), 9.8 g of 37% formaldehyde (Sigma Aldrich, ACS Reagent), 4.1 g of water (18 MΩ cm, Barnstead Nanopure water system), and 0.013 g of sodium carbonate (Sigma Aldrich, ACS Reagent) were combined in a glass vial. The solution was stirred for 30 min and then allowed to stand for 2.5 h. Lydall Technimat (density, 0.2 g cm^{-3}; 90-μm thick) carbon fiber-paper was cut into a 4×4 cm^2 piece, immersed in the aged RF solution, and vacuum infiltrated. The RF sol-infiltrated carbon fiber paper was sandwiched between two 5×5 cm^2 glass slides and sealed in duct tape. The sealed samples were placed inside a pressure cooker (Nesco 3-in-1 pressure cooker) at ~90 °C for 9.5 h, after which, the samples were removed from the glass slide assembly, soaked in water for 1 h, followed by soaking in acetone for 1 h. The samples were removed from the acetone and allowed to dry under ambient laboratory conditions for 2 h. The RF-nanofoam papers were pyrolyzed under flowing argon (100 mL min^{-1}) in a tube furnace. Pyrolysis was achieved by ramping the temperature at 1 °C min^{-1} to 1000 °C, holding at 1000 °C for 2 h, and ramping down at 1 °C min^{-1} to 25 °C.

Electroless Deposition of FeOx on Carbon Nanofoams. Carbon nanofoams were placed in a plastic vial and vacuum infiltrated with 9 M KOH (Sigma Aldrich) and soaked for 24 h. The KOH-infiltrated carbon nanofoams were then soaked in 25 mM K_2FeO_4 (Sigma Aldrich) in 9 M KOH under vacuum for 20 h. After deposition, the FeO_x-carbon nanofoam papers were rinsed thoroughly with water and then soaked in fresh water under vacuum for three 1-h periods. The FeO_x-carbon nanofoams were subsequently dried at ~50 °C under N_2 for 8 h and then under vacuum overnight. To increase the weight loading, 20-h FeO_x samples were subjected to a cleaning step that involved infiltrating the FeO_x-nanofoam with 70 °C water and soaking for 6 h. The "cleaned" 20-h FeO_x-carbon samples were then dried under N_2 at 50 °C for 8 h. The cleaned 20-h FeO_x-carbon samples were then infiltrated with 9 M KOH for 24 h followed by soaking in 25 mM K_2FeO_4 in 9 M KOH for 20 h to bring the total deposition time to 40 h. Select FeO_x-carbon nanofoams were submitted to Galbraith Laboratories (Knoxville, TN) to determine the C, Fe, and K content. Surface area and pore structure were determined by nitrogen-sorption porosimetry (Micrometrics ASAP2010). Prior to analysis, samples were degassed at 150 °C under vacuum for 24 h.

Electrochemical Characterization. Electrodes were fabricated by adhering a preweighed piece (typically 1 cm $\times$ 1 cm) of the FeO_x-carbon nanofoam to a nickel foil (Alfa Aesar, 100-μm thick) flag with nickel print (MG Chemicals). Epoxy (Loctite 1C) was used to cover exposed areas of the nickel foil. The electrode was vacuum-infiltrated with aqueous 2.5 M Li_2SO_4 (Fluka) prior to electrochemical experiments. Electrochemical measurements were performed in a conventional three-electrode electrochemical cell with a Pt-mesh auxiliary electrode and a Ag/AgCl (World Precision Instruments) reference electrode using a Voltalab 40 potentiostat/galvanostat (Radiometer Analytical). Prior to electrochemical experiments, the electrolyte was degassed with nitrogen for 30 min and then blanketed with nitrogen for the remainder of the experiment.

Electron Microscopy. A Zeiss Supra55 scanning electron microscope (20 kV) was used to examine the exterior and interior surfaces of bare and FeO_x-coated carbon nanofoams. For exterior surface imaging, a small piece of the nanofoam was adhered to an aluminum SEM stub with conductive carbon tape (Ted Pella). For interior surface imaging, the nanofoam was sliced in half with a new razor blade and mounted on an aluminum 45°/90° vertical SEM stub with conductive carbon tape. A Princeton Gamma Tech EDS system was used for energy-dispersive X-ray analysis. A JEOL 2200FS transmission electron microscope (TEM) equipped with a Gatan CCD camera was used to characterize the FeO_x-carbon morphologies and confirm the FeO_x distribution. Samples were prepared by dry-grinding the nanofoam then brushing the dust onto holey-carbon film support grids. Multiple areas for each sample were investigated to ensure that the images we obtain are representative of the whole sample.

X-ray Absorption Spectroscopy. The XAS experiments were conducted on the bending magnet station X-11A of the National Synchrotron Light Source at Brookhaven National Laboratory with the electron storage ring operating at electron energy of 2.8 GeV and a stored current in the range of 200—300 mA.[44] The Fe K-edge X-ray absorption fine structure (XAFS) spectra were collected at room temperature in transmission mode using two flat Si(111) double crystal monochromator. The harmonic content of the beam was minimized by adjusting the parallelism of the monochromator crystals to reduce the peak intensity by 40%. The incident and transmitted beam intensities were monitored using ionization chambers with the appropriate combination of nitrogen, helium, or argon flowing through the chambers. Further details are provided in the Supporting Information.

Supporting Information Available: Elemental analysis, weight loading calculation, X-ray photoelectron C1s spectra, cyclic voltammograms, Nyquist plots, *in situ* XAS/electrochemical cell design, further details on the XAS measurements, and data analysis methods, as well as XAS data as a function of electrochemical cycling, additional HR-TEM images, photograph of qualitative colorimetric analysis, and a table of the electrochemical and physical properties of iron oxide-based electrodes reported in

the literature. This material is available free of charge *via* the Internet at http://pubs.acs.org.

REFERENCES AND NOTES

1. Koksbang, R.; Barker, J.; Shi, H.; Saïdi, M. Y. Cathode Materials for Lithium Rocking Chair Batteries. *Solid State Ionics* **1996**, *84*, 1–21.
2. Manthiram, A.; Kim, J. Low Temperature Synthesis of Insertion Oxides for Lithium Batteries. *Chem. Mater.* **1998**, *10*, 2895–2909.
3. Jiang, C.; Hosono, E.; Zhou, H. Nanomaterials for Lithium Ion Batteries. *NanoToday* **2006**, *1*, 28–33.
4. Shukla, A. K.; Prem Kumar, T. Materials for Next-Generation Lithium Batteries. *Curr. Sci.* **2008**, *94*, 314–331.
5. Bruce, P. G.; Scrosati, B.; Tarascon, J.-M. Nanomaterials for Rechargeable Lithium Batteries. *Angew. Chem., Int. Ed.* **2008**, *47*, 2930–2946.
6. Conway, B. E. Transition from "Supercapacitor" to "Battery" Behavior in Electrochemical Energy Storage. *J. Electrochem. Soc.* **1991**, *138*, 1539–1548.
7. Burke, A. Ultracapacitors: Why, How, and Where is the Technology. *J. Power Sources* **2000**, *91*, 37–50.
8. Huggins, R. A. Supercapacitors and Electrochemical Pulse Sources. *Solid State Ionics* **2000**, *134*, 179–195.
9. Zheng, J. P.; Cygan, P. J.; Jow, T. R. Hydrous Ruthenium Oxide as an Electrode Material for Electrochemical Capacitors. *J. Electrochem. Soc.* **1995**, *142*, 2699–2703.
10. Doherty, C. M.; Caruso, R. A.; Smarsly, B. M.; Adelhelm, P.; Drummond, C. J. Hierarchically Porous Monolithic LiFePO$_4$/Carbon Composite Electrode Materials for High Power Lithium Ion Batteries. *Chem. Mater.* **2009**, *21*, 5300–5306.
11. Armstrong, A. R.; Tee, D.; La Mantia, F.; Novák, P.; Bruce, P. G. Synthesis of Tetrahedral LiFeO$_2$ and Its Behavior as a Cathode in Rechargeable Lithium Batteries. *J. Am. Chem. Soc.* **2008**, *130*, 3554–3559.
12. Hibino, M.; Terashima, J.; Yao, T. Reversible and Rapid Discharge–Charge Performance of γ-Fe$_2$O$_3$ Prepared by Aqueous Solution Method as the Cathode for Lithium-Ion Battery. *J. Electrochem. Soc.* **2007**, *154*, A1107–A1111.
13. Amine, K.; Yasuda, H.; Yamachi, M. β-FeOOH, A New Positive Electrode Material for Lithium Secondary Batteries. *J. Power Sources* **1999**, *81–82*, 221–223.
14. Xu, J. J.; Jain, G. A Nanocrystalline Ferric Oxide Cathode for Rechargeable Lithium Batteries. *Electrochem. Solid-State Lett.* **2003**, *6*, A190–A193.
15. Jain, G.; Balasubramanian, M.; Xu, J. J. Structural Studies of Lithium Intercalation in a Nanocrystalline α-Fe$_2$O$_3$ Compound. *Chem. Mater.* **2006**, *18*, 423–434.
16. Jain, G.; Capozzi, C. J.; Xu, J. J. Nanosized Amorphous Iron Oxyhydroxide for Reversible Lithium Intercalation. *J. Electrochem. Soc.* **2003**, *150*, A806–A810.
17. Sarradin, J.; Ribes, M.; Guessous, A.; Elkacemi, K. Study of Fe$_2$O$_3$-Based Thin Film Electrodes for Lithium-Ion Batteries. *Solid State Ionics* **1998**, *112*, 35–40.
18. Reddy, M. V.; Yu, T.; Sow, C.-H.; Shen, Z. X.; Lim, C. T.; Subba Rao, G. V.; Chowdari, B. V. R. α-Fe$_2$O$_3$ Nanoflakes as an Anode Material for Li-Ion Batteries. *Adv. Funct. Mater.* **2007**, *17*, 2792–2799.
19. Wu, N.-L.; Wang, S.-Y.; Han, C.-Y.; Wu, D.-S.; Shiue, L.-R. Electrochemical Capacitor of Magnetite in Aqueous Electrolytes. *J. Power Sources* **2003**, *113*, 173–178.
20. Nagarajan, N.; Zhitomirsky, I. Cathodic Electrosynthesis of Iron Oxide Films for Electrochemical Supercapacitors. *J. Appl. Electrochem.* **2006**, *36*, 1399–1405.
21. Jin, W.-H.; Cao, G.-T.; Sun, J.-Y. Hybrid Supercapacitor Based on MnO$_2$ and Columned FeOOH Using Li$_2$SO$_4$ Electrolyte Solution. *J. Power Sources* **2008**, *175*, 686–691.
22. Cottineau, T.; Toupin, M.; Delahaye, T.; Brousse, T.; Bélanger, D. Nanostructured Transition Metal Oxides for Aqueous Hybrid Electrochemical Supercapacitors. *Appl. Phys. A: Mater. Sci. Process.* **2006**, *82*, 599–606.
23. Brousse, T.; Bélanger, D. A Hybrid Fe$_3$O$_4$-MnO$_2$ Capacitor in Mild Aqueous Electrolyte. *Electrochem. Solid State Lett.* **2003**, *6*, A244–A248.
24. Chung, K. W.; Kim, K. B.; Han, S.-H.; Lee, H. Novel Synthesis and Electrochemical Characterization of Nano-Sized Cellular Fe$_3$O$_4$ Thin Film. *Electrochem. Solid-State Lett.* **2005**, *8*, A259–A262.
25. Wu, M.-S.; Lee, R.-H.; Jow, J.-J.; Yang, W.-D.; Hsieh, C.-Y.; Weng, B.-J. Nanostructured Iron Oxide Films Prepared by Electrochemical Method for Electrochemical Capacitors. *Electrochem. Solid-State Lett.* **2009**, *12*, A1–A4.
26. Fischer, A. E.; Pettigrew, K. A.; Rolison, D. R.; Stroud, R. M.; Long, J. W. Incorporation of Homogeneous, Nanoscale MnO$_2$ within Ultraporous Carbon Structures *via* Self-Limiting Electroless Deposition: Implications for Electrochemical Capacitors. *Nano Lett.* **2007**, *7*, 281–286.
27. Fischer, A. E.; Saunders, M. P.; Pettigrew, K. A.; Rolison, D. R.; Long, J. W. Electroless Deposition of Nanoscale MnO$_2$ on Ultraporous Carbon Nanoarchitectures: Correlation of Evolving Pore-Solid Structure and Electrochemical Performance. *J. Electrochem. Soc.* **2008**, *155*, A246–A252.
28. Sharma, V. K. Potassium Ferrate (VI): An Environmentally Friendly Oxidant. *Adv. Environ. Res.* **2002**, *6*, 143–156.
29. Yuan, P.; Wu, Q.; Ding, Y.; Wu, H.; Yang, X. One-Step Synthesis of Iron-Oxide-Loaded Functionalized Carbon Spheres. *Carbon* **2009**, *47*, 2648–2654.
30. Pekala, R. W.; Farmer, J. C.; Alviso, C. T.; Tran, T. D.; Mayer, S. T.; Miller, J. M.; Dunn, B. Carbon Aerogels for Electrochemical Applications. *J. Non-cryst. Solids* **1998**, *225*, 74–80.
31. Lytle, J. C.; Barrow, A. J.; Saunders, M. P.; Long, J. W.; Dysart, J. L.; Rolison, D. R. Macroporous Carbon Nanofoam Composites and Methods of Making Same. U.S. Patent Application S/N 12/620,541, Nov. 17, 2009.
32. Mao, W.; Wang, J.; Xu, Z.; Niu, Z.; Zhang, J. Effects of the Oxidation Treatment with K$_2$FeO$_4$ on the Physical Properties and Electrochemical Performance of a Natural Graphite as Electrode Material for Lithium Ion Batteries. *Electrochem. Commun.* **2006**, *8*, 1326–1330.
33. Wu, M.-S.; Lee, R.-H. Electrochemical Growth of Iron Oxide Thin Films with Nanorods and Nanosheets for Capacitors. *J. Electrochem. Soc.* **2009**, *156*, A737–A743.
34. Rolison, D. R.; Long, J. W.; Lytle, J. C.; Fischer, A. E.; Rhodes, C. P.; McEvoy, T. M.; Bourg, M. E.; Lubers, A. M. Multifunctional 3D Nanoarchitectures for Energy Storage and Conversion. *Chem. Soc. Rev.* **2009**, *38*, 226–252.
35. Zhang, L. L.; Zhao, X. S. Carbon-Based Materials as Supercapacitor Electrodes. *Chem. Soc. Rev.* **2009**, *38*, 2520–2531.
36. Qu, Q. T.; Wang, B.; Yang, L. C.; Shi, Y.; Tian, S.; Wu, Y. P. Study on Electrochemical Performance of Activated Carbon in Aqueous Li$_2$SO$_4$, Na$_2$SO$_4$, and K$_2$SO$_4$ Electrolytes. *Electrochem. Commun.* **2008**, *10*, 1652–1655.
37. Andreas, H. A.; Conway, B. E. Examination of the Double-Layer Capacitance of a High Specific-Area C-Cloth Electrode as Titrated from Acidic to Alkaline pHs. *Electrochim. Acta* **2006**, *51*, 6510–6520.
38. Schmuki, P.; Virtanen, S.; Davenport, A. J.; Vitus, C. M. *In Situ* X-ray Absorption Near-Edge Spectroscopic Study of the Cathodic Reduction of Artificial Iron Oxide Passive Films. *J. Electrochem. Soc.* **1996**, *143*, 574–582.
39. Manceau, A.; Gorshkov, A. I.; Drits, V. A. Structural Chemistry of Mn, Fe, Co, and Ni in Manganese Hydrous Oxides; Part I, Information from XANES Spectroscopy. *Am. Mineral.* **1992**, *77*, 1133–1143.
40. Westre, T. E.; Kennepohl, P.; DeWitt, J. G.; Hedman, B.; Hodgson, K. O.; Solomon, E. I. A Multiplet Analysis of Fe K-Edge 1s $\rightarrow$ 3d Pre-edge Features of Iron Complexes. *J. Am. Chem. Soc.* **1977**, *119*, 6297–6314.
41. Mancey, D. S.; Shoesmith, D. W.; Lipkowski, J.; McBride, A. C.; Noël, J. An Electrochemical Investigation of the Dissolution of Magnetite in Acidic Electrolytes. *J. Electrochem. Soc.* **1993**, *140*, 637–642.
42. Grygar, T. Electrochemical Dissolution of Iron (III) Hydroxy-oxides: More Information About the Particles. *Collect. Czech. Chem. Commun.* **1996**, *61*, 93–106.
43. Zboril, R.; Mashlan, M.; Petridis, D. Iron (III) Oxides from Thermal Processes: Synthesis, Structural and Magnetic

Properties, Mössbauer Spectroscopy Characterization, and Applications. *Chem. Mater.* **2002**, *14*, 969–982.

44. Sayers, D. E.; Heald, S. M.; Pick, M. A.; Budnick, J. I.; Stern, E. A.; Wong, J. X-ray Beam Line at the NSLS for X-ray Absorption Studies in Material Science. *Nucl. Instrum. Methods Phys. Res.* **1983**, *208*, 631–635.